ACS OMEGA

http://pubs.acs.org/journal/acsodf

Article

Simultaneous Electrodeposition of Ternary Metal Oxide Nanocomposites for High-Efficiency Supercapacitor Applications

Eshetu Mekonnen Abebe and Masaki Ujihara*

Cite This: *ACS Omega* 2022, 7, 17161−17174

Read Online

ACCESS | Metrics & More | Article Recommendations | Supporting Information

ABSTRACT: Complex oxides and hydroxides of Ni, Co, and Mn from a precursor mixture were electrochemically deposited on both a cathode and an anode. On the Ni foam cathode, the complex metal hydroxides precipitated as nanolayers at −0.9 V. Simultaneously, the metal ions were oxidized and deposited as blocks on the Ni foam anode. While the concentrations of $Ni(NO_3)_2$ and $Mn(NO_3)_2$ were constant (80 mM for Ni^{2+} and 40 mM for Mn^{2+}, respectively), the concentration of $Co(NO_3)_2$ was varied from 20 to 120 mM, which affected the morphology and electrochemical properties of the electrode: a Co:Ni:Mn molar ratio resulted in the highest specific capacitance (at a scan rate of 5 mV s^{-1}, 1800 F g^{-1} for the cathode material and 720 F g^{-1} for the anode material). This cathode material was assembled into symmetric supercapacitors, which demonstrated an excellent energy density of 39 Wh kg^{-1} at a power density of 1300 W kg^{-1} and a high capacitance retention of 90% after 3000 charge/discharge cycles. This high electrochemical performance was attributed to the optimized ratio of metal oxides, and this simple preparation strategy can be applied to other nanocomposites of complex metal oxides/hydroxides with desired characteristics for various applications.

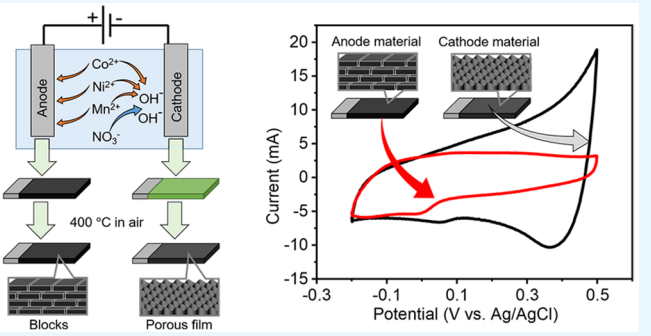

1. INTRODUCTION

Electrochemical capacitors have attracted the attention of researchers in recent decades as a major key to meeting the growing demands of energy storage and conversion due to their high power density, rapid charge−discharge rate, broad operating temperature ranges, and long life cycles, thus filling the gap between conventional capacitors and batteries.[1−3] These benefits give supercapacitors enormous potential for utilization in next-generation environmentally friendly energy conversion and storage devices, especially in transportation, electronic products, smart grids, and aerospace applications.[4]

Supercapacitors can be categorized into three broad classes: electrochemical double-layer capacitors (EDLCs, non-Faradaic), pseudocapacitors (Faradaic), and hybrid capacitors (combinations of the other two).[5,6] In pseudocapacitors, electrodes are reduced/oxidized to store electrical energy, and therefore, the electrode materials should be reactive over the proper range of potentials, stable to reversible reactions, and mechanically stable during redox processes. Considering the stability of the whole system, the difference in potential between electrodes is also limited to <1.8 V in acid/alkaline aqueous media or ∼2 V in neutral media.[7] To satisfy such requirements, transition metal oxides (TMOs) can be used as electrode materials for energy storage. Several metals have been examined, not only because of their redox properties but also because of their abundance and environmental friendliness for practical applications. Currently, Mn, Fe, Ni, Co, and W are frequently used as active materials in pseudocapacitor electrodes.[8−10] These TMOs have high theoretical specific capacitance, and their electrochemical performance can be enhanced by controlling and adjusting the morphologies and structure to the nanoscale. On the other hand, their low electrical conductivity, volume expansion during charge/discharge, and stagnant ion movement in the bulk phase limit their practical applications. To overcome these limitations, many researchers have reported the use of inexpensive composites of TMOs with conductive polymers,[11] carbon materials,[12] and secondary metal oxides.[13] It should also be noted that these metallic species are known as electrochemical catalysts, and the effects of chemical states and nanostructures on electrochemical reactions such as water electrolysis should be considered for their usage in aqueous media.[14,15]

Among these composites, complex TMOs can improve the electrochemical performance compared to single constituents due to their enhanced electrical conductivity, physical and

Received: February 10, 2022
Accepted: May 4, 2022
Published: May 14, 2022

chemical stability, abundant active sites for redox reactions, shape control, and other synergetic effects.[16−19] Currently, nickel, cobalt, and manganese are widely used to prepare TMO nanocomposites with different morphologies suitable for pseudocapacitors. To prepare complex TMOs for pseudocapacitors, stepwise deposition can be applied. In our previous study, ZnO nanotubes were first deposited, and then secondary Co hydroxide nanoplates were hybridized.[20] In this study, the simultaneous deposition of Zn and Co hydroxide/oxide was not effective because the structure of the obtained Zn/Co oxides was not adequate for rapid ion adsorption/desorption and charge transfer. The simultaneous deposition of multiple metal ions is a simple method; however, investigations of the simultaneous deposition of complex TMOs for pseudocapacitor electrodes are rare. MnO_2 and $Mn(OH)_2$ were synthesized simultaneously using the electrodeposition method from a single electrolyte and reported as promising electrodes for supercapacitor applications.[21] Double-shelled tremella-like $NiO@Co_3O_4@MnO_2$ as a high-performance supercapacitor with a specific capacitance of 792 F g^{-1} was reported by Hui Wang et al.[22] A flexible and binder-free PPy and MnO_2 electrode was also simultaneously prepared as a supercapacitor electrode using a simple electrodeposition method.[11] The electrochemically deposited $Mn(OH)_2$ formed nanoplates, which could be suitable for pseudocapacitors and further calcined to Mn oxides.

However, the effect of simultaneous deposition of $NiO@Co_3O_4@MnO_2$ as the cathode and anode material and the precise optimum ratios of the Co^{2+} reactant remain unidentified. Electrochemical deposition is a promising method to simultaneously prepare complex TMOs from mixtures of corresponding precursors, and the chemical states of the obtained TMOs can be controlled by the applied potential.

In this study, we electrochemically prepared complex TMOs on the cathode and anode simultaneously from a precursor solution containing a mixture of nickel, cobalt, and manganese salts. Compared to the anode material, the cathode material had a larger surface area due to nanolayer structures and exhibited high electrochemical performance. Here, to our knowledge, a simple, efficient, and cost-effective solution-reaction method for the simultaneous synthesis of complex TMOs with different nanostructures and high electrochemical supercapacitive performance has been reported for the first time. Both the cathode and anode materials possessed different morphologies and exhibited high specific capacitances of 1800 F g^{-1} and 720 F g^{-1} at 5 mV s^{-1}, respectively. A symmetric supercapacitor with a KOH electrolyte was further assembled to demonstrate an opportunity for a facile and effective energy storage device using the approach described in this study.

2. EXPERIMENTAL SECTION

2.1. Materials. The reagents nickel(II) nitrate hexahydrate ($Ni(NO_3)_2·6H_2O$, Alfa), cobalt(II) nitrate hexahydrate ($Co(NO_3)_2·6H_2O$, Acros), manganese(II) nitrate tetrahydrate ($Mn(NO_3)_2·4H_2O$, Alfa Aesar), sodium nitrate ($NaNO_3$, Acros), and potassium hydroxide (KOH, Fisher Chemical) were of analytic grade and were used as received without further purification. Nickel foam (110 PPI, approximately 1.7 mm × 1 cm × 3 cm, Fucell CO., Ltd.) was washed with 6 M hydrochloric acid solution (HCl, Fisher Chemical) in an ultrasonic bath for 30 min to remove the NiO layer on the surface and then subsequently rinsed with deionized water and isopropanol (Acros Organics) for 10 min in an ultrasonic bath and dried at room temperature. The Ni foam was covered with a Kapton film with adhesive to control the surface area to be exposed to the electrolyte solution. Throughout the experiments, ultrapure water with a resistivity of 18.2 MΩ·cm (Yamato, Japan) was used.

2.2. Electrochemical Deposition. For electrochemical deposition, a potentiostat/galvanostat (Hokuto-Denko, model HA-151B, Japan) was used. The electrolyte solution for deposition was prepared from a powder of $Ni(NO_3)_2·6H_2O$, $Co(NO_3)_2·6H_2O$, and $Mn(NO_3)_2·4H_2O$ dissolved in 50 mL of deionized water. The Ni^{2+} (80 mM) and Mn^{2+} (40 mM) concentrations were fixed, whereas that of Co^{2+} was varied (20, 40, 80, and 120 mM). Electrodeposition was carried out in a standard three-electrode glass cell consisting of two pieces of precleaned Ni foam with an apparent exposed area of 2 cm^2 as the working electrode and counter electrode and Ag/AgCl in a saturated KCl solution as the reference electrode. From the electrolyte solution, deposition was performed at a potential of −0.90 V vs Ag/AgCl. After deposition for 5 min, a greenish material was directly deposited on the working electrode (cathode), and a black material was formed on the counter electrode (anode). Then, the obtained samples (both the cathode and the anode materials) were rinsed with water to remove any residual electrolyte and dried at 100 °C for 30 min, followed by calcination at 400 °C for 1 h on a hot plate. The mass of each deposited material was calculated by subtracting the weight of the electrode before and after the deposition. The weight was measured to the order of 0.01 mg and rounded off to two significant digits.

2.3. Material Characterization. The surface morphology of the deposited materials on the Ni foam was revealed by scanning electron microscopy (SEM) at an acceleration rate of 5 kV using field emission scanning electron microscopy (FE-SEM; JEOL JSM-6500F). The elemental composition was analyzed with energy dispersive X-ray spectroscopy (EDS) at an acceleration rate of 10 kV using FE-SEM equipment. Fourier transform infrared (FTIR) absorption spectra of the deposited materials were recorded in the range 500−4000 cm^{-1} using the KBr plate method using a Nicolet Thermo Scientific 6700 spectrometer. The crystal structure of the deposited materials was recorded using X-ray diffraction (XRD, Bruker, D2 phaser USA) with Cu Kα radiation (1.54 Å) at 40 kV and 30 mA at room temperature with a step size of 0.05° and a step time of 5 s in the 2θ range 10−80°. The chemical state and elemental valence state of the samples were characterized using X-ray photoelectron spectrometry (XPS, Auger electron microbe (VG Scientific Microlab 350) with an EX05 ion gun (5 kV, maximum beam current >5 μA at 4 kV).

2.4. Electrochemical Measurement. Electrochemical measurements were performed in a 1 M KOH aqueous electrolyte solution using a three-electrode cell consisting of a deposited material/Ni foam as the working electrode, platinum wire as the counter electrode, and Ag/AgCl in a saturated KCl solution as the reference electrode on an electrochemical workstation (ZAHNER mess system, model XPot-26366, Germany). Cyclic voltammetry (CV), galvanostatic charging/discharging (GCD), and cycling tests were conducted over the potential range −0.2 to 0.5 V vs Ag/AgCl. Electrochemical impedance spectroscopy (EIS) measurements were carried out in the frequency range 10 mHz to 100 kHz with a perturbation amplitude of 10 mV at the open circuit potential. To evaluate the practical applicability, a symmetric supercapacitor was

https://doi.org/10.1021/acsomega.2c00826
ACS Omega 2022, 7, 17161−17174

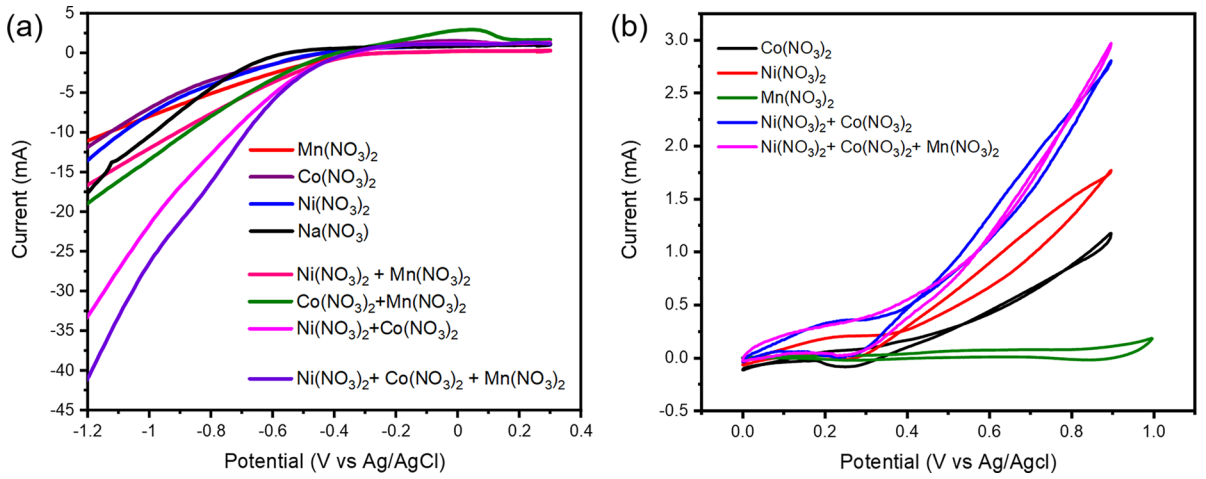

Figure 1. (a) Cathodic polarization curves of a nickel foam electrode in nitrate solutions. (b) CV curves at the scan rate 10 mV s^{-1}. For each metal species, the concentration was 40 mM.

fabricated by assembling two electrodes both made of cathode material with a comparable mass. Filter paper (Whatman, pore size 0.45 μm) was immersed in a 1 M KOH aqueous electrolyte and assembled as a separator before the electrochemical measurements. Then, CV curves of the two-electrode system were recorded at different potential ranges from −0.4 to 0.4 V and from −0.8 to 0.8 V at 20 mV s^{-1}.

3. RESULTS AND DISCUSSION

3.1. Electrochemical Reactions of Precursor Solutions. Prior to the electrodeposition of the complex TMOs, the components of the TMOs were first characterized by both the cathodic and anodic polarization curves of the corresponding precursor solution (Figure 1).

Cathodic polarization was performed in the potential window from −2.0 to 0.3 V vs Ag/AgCl at the scan rate 10 mV s^{-1}. For all species, the current was nearly zero in the potential range from −0.3 to 0.3 V vs Ag/AgCl, while $Na(NO_3)_2$ as a control exhibited zero current between −0.5 and 0.3 V vs Ag/AgCl. At lower than −0.3 V vs Ag/AgCl, the reduction current increased as the potential shifted lower, which may be mainly due to the reduction of nitrate ions, since these metal ions cannot be reduced at higher than −0.9 V vs Ag/AgCl (−1.1 V vs SHE).[23] Compared with the $Na(NO_3)$ solution, the solutions of transition metal ions (Ni^{2+}, Co^{2+}, and Mn^{2+}) exhibited higher current in this range (−0.3 to −0.9 V vs Ag/AgCl), which suggested that these metal species promoted the reduction of nitrate ions. The polarization curve of Ni^{2+} shifted slightly to a more positive potential than those of other transition metals (Figure 1a). For the mixture of Co^{2+} and Ni^{2+}, the polarization curve shifted to a more positive potential in the cathodic reactions. The addition of Mn^{2+} resulted in the most positive potential for the polarization curve. At −0.9 V vs Ag/AgCl, the current values for both 40 mM $Co(NO_3)_2$ and $Ni(NO_3)_2$ electrolytes were nearly 5.10 mA, and that of the mixture of $Ni(NO_3)_2$ and 40 mM $Co(NO_3)_2$ was 16.88 mA. The mixture of 40 mM $Ni(NO_3)_2$, 40 mM $Co(NO_3)_2$, and 40 mM $Mn(NO_3)_2$ resulted in a current value of 21.03 mA. This increase in current was attributed to the increase in concentrations of NO_3^- ions in the solutions; however, the current was not proportional to the concentration of NO_3^- ions. Then, a synergistic effect of the metals involved in the electrolytic activities was suggested, especially for the mixture of Ni^{2+} and Co^{2+}.[24,25]

On the other hand, the anodic current for single components, Co^{2+} and Ni^{2+}, increased slowly at potentials greater than 0.2 V vs Ag/AgCl (Figure 1b). The mixture of Co^{2+} and Ni^{2+} and the mixture of three metal ions resulted in a steeper increase in the anodic current. These anodic currents suggested that the oxidation of these metal ions took place at potentials >0.2 V vs Ag/AgCl. Compared to these ions, Mn^{2+} was less active for the anodic reaction. The currents reached 1.76, 1.17, and 0.17 mA at 0.9 V vs Ag/AgCl for single-component solutions of Ni^{2+}, Co^{2+}, and Mn^{2+} precursors, respectively. For the mixture of Co^{2+} and Ni^{2+}, the current was enhanced to 2.80 mA, which corresponded to the sum of anodic currents from individual components. For the mixture of three metal ions, the current reached 2.97 mA. These results suggest that mixing different metal ions had an additive effect on the oxidation reaction. To balance the currents on the cathode at −0.9 V, the anode potential should be higher than the range measured in this study.

3.2. Electrodeposition and Calcination of Cathode and Anode Materials. The electrodeposition of the cathode and anode materials was conducted using electrolyte solutions consisting of three metal precursors (nitrates of Ni^{2+}, Co^{2+}, and Mn^{2+}). At the cathode, nitrate ions (NO_3^-) were reduced to produce hydroxide ions (OH^-), which reacted with M^{2+} ions to form metal hydroxides on the Ni foam.[2] Visually, the hydroxides deposited on the Ni foam were observed as green materials (Figure S1 in the Supporting Information). After heat treatment at 400 °C, the green materials were converted into black materials, which were thought to be the complex TMOs formed by air oxidation. On the other hand, the deposited materials on the anode were black before calcination (Figure S2). The metal ions were electrochemically oxidized to precipitate their insoluble metal oxides and oxyhydroxides on the anode. Typically, at neutral pH, Co^{2+} ions can be oxidized to form Co_3O_4 or $CoO(OH)$;[26,27] Ni^{2+} ions can be oxidized to form $NiO(OH)$;[28] and Mn^{2+} can be oxidized to form $MnOOH$, Mn_2O_3, Mn_3O_4, $MnO(OH)_2$, and MnO_2.[11,21] Hereafter, the cathode materials after calcination were named cathode-1, cathode-2, cathode-3, and cathode-4, and the corresponding anode materials were named anode-1, anode-

https://doi.org/10.1021/acsomega.2c00826
ACS Omega 2022, 7, 17161−17174

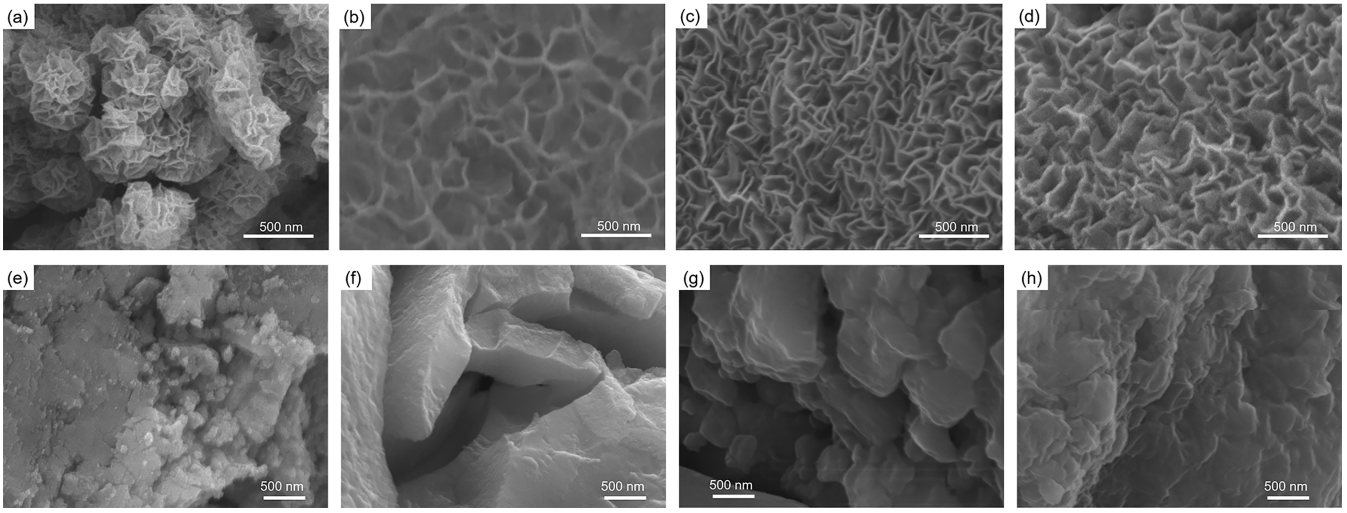

Figure 2. SEM image of cathode materials: (a) cathode-1, (b) cathode-2, (c) cathode-3, (d) cathode-4, (e) anode-1, (f) anode-2, (g) anode-3, and (h) anode-4.

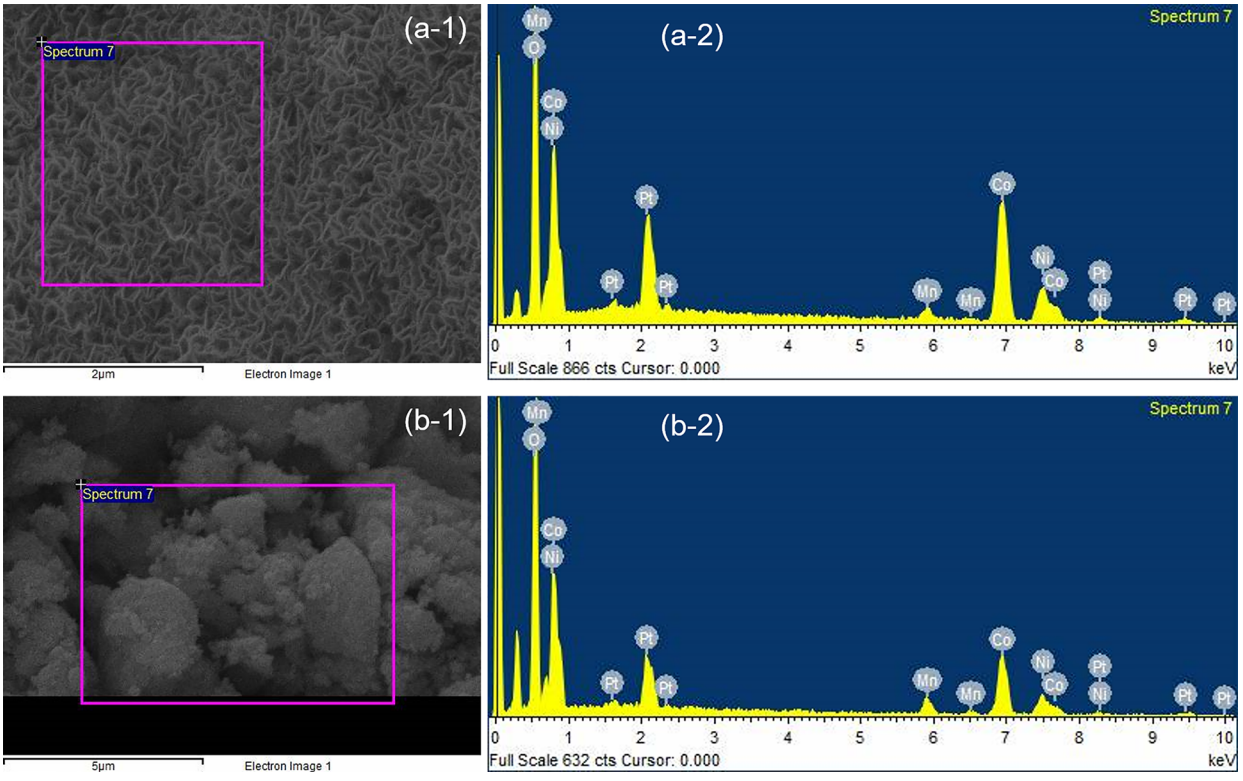

Figure 3. SEM images of (a-1) cathode-3 and (b-1) anode-3 and their EDS spectra (a-2 for cathode-3 and b-2 for anode-3).

2, anode-3, and anode-4 for the sample prepared using precursor Co^{2+} at 20, 40, 80, and 120 mM, respectively.

3.3. Morphological and Structural Characterization. The morphology of both the cathode and anode materials was observed by SEM (Figure 2). The cathode materials exhibited nanosheet structures and changed their morphologies from spherical nanoflowers (cathode-1) to flat porous films as the concentration of the Co^{2+} precursor increased, as reported previously for Mn oxides and Co oxides.[11,20] The nanosheets of cathode-3 had a mean thickness and length of ∼10 and 197 nm, respectively, and interconnected with each other. The thickness and length of the nanosheets increased and decreased (to ∼22 and 87 nm), respectively, as the precursor concentration of Co^{2+} increased to 120 mM (cathode-4); that is, the network density of the metal oxides increased. These nanosheet formations are advantageous for applications in electrochemical devices since the open space between each nanosheet provides effective transport of electrolyte ions into the inner surface of the electrode, which can enhance the rapid diffusion of electrolyte and decrease the internal resistance.[29,30] Interestingly, the nanosheets were interconnected with each other and formed network structures, which enabled electron movement throughout the nanosheet network.

Furthermore, the morphology of the anode materials was different from that of the cathode materials (Figure 2e,f). The anode materials were generally observed as blocks with

https://doi.org/10.1021/acsomega.2c00826
ACS Omega 2022, 7, 17161−17174

powders. This structure suggests that the oxidation and deposition of metal ions could simultaneously occur on the electrode: since the conductivity of metal oxides was low, the oxidation reaction preferentially occurred at the thinner part in the film, and then the metal oxide formed at the thinner part filled up the pocket to make the film flat. Although cracks and powders could be formed by the drying process, the surface area of the anode materials is expected to be low.

The elemental compositions of the cathode-3 and anode-3 nanocomposites were assessed using EDS (Figure 3). The EDS spectra of both nanocomposites clearly showed the presence of Co, Ni, Mn, and O. (An additional peak due to the platinum coating used for SEM measurement was also observed.) The atomic weight percentage of each element confirmed the successful synthesis of cathode-3 and anode-3 on the Ni foam (Table 1). The molar ratio of these elements in the precursor solution was 2:2:1 for Ni, Co, and Mn. In the cathode and anode materials, the ratios of the metal species were similar: the amount of Co was the highest, and that of Mn was the lowest. The deviation of the molar ratios of cathode/anode materials from the precursor ratio could be due to many factors, such as the solubility of metal hydroxides (for cathode materials) and redox potentials (for anode materials); however, these results are consistent with the results of electrochemical reactions of precursor solutions in terms of the synergetic reaction of Co^{2+} and Ni^{2+} and the low efficiency of Mn^{2+}.

Table 1. Elemental Compositions of the Cathode and Anode Materials

	atomic weight percentage of elements			
sample	Co	Ni	Mn	O
cathode-3	30.95	10.37	1.32	54.58
anode-3	28.82	7.76	3.02	58.5

3.4. Chemical States and Crystallinity of the Cathode and Anode Materials. The FTIR spectra of the cathode and anode materials are shown in Figure 4a. The wide band at approximately 3460 cm^{-1} for both cathode-3 and anode-3 was ascribed to the O−H stretching vibration mode.[31] The weak band at approximately 1625 cm^{-1} for the cathode and anode films was assigned to the bending vibration of the O−H groups with metal atoms.[32] The peaks at approximately 1140 and 921 cm^{-1} were attributed to the bending vibration of -OH groups combined with metal atoms and could be due to O−H stretching vibrations.[33,34] The broad peak at approximately 1114−1178 cm^{-1} (centered at 1140 cm^{-1}) for the anode suggested disordered structures or hydrogen bonding interactions. Thus, hydrated properties were suggested for both materials. The strong sharp peak at 1384 cm^{-1} was attributed to the stretching vibration of NO_3^-, which is due to the residue of nitrate ions, and the high intensity of this peak indicates a significant amount of nitrate ions in the materials.[35,36] The bands in the range from 400 to 600 cm^{-1} were assigned to stretching vibration modes of metal−oxygen bonds. In detail, stretching vibration modes appeared at 586, 520, and 457 cm^{-1}, corresponding to Co−O, Mn−O, and Ni−O, respectively.[33,37]

The XRD spectra of the cathode and anode electrodes are shown in Figure 5b. The strong peaks for both electrodes at 44.78°, 52.19°, and 76.59° were assigned to the (111), (200), and (220) planes, respectively, of metallic nickel, which come from the Ni foam substrate (JCPDS-2865). For both the cathode and anode materials, diffraction peaks centered at 31.57°, 36.74°, 59.40°, and 77.80° were observed, and they were indexed to the lattices of (220), (311), (224), and (226) of the spinal Co_3O_4 crystal structure, respectively (JCPDS card no. 42-1467). However, the peaks at 38.67°, 43.3°, and 73.86° corresponded to the (111), (200), and (220) planes of the face-centered cubic phase of NiO (JCPDS card no. 47-1049). For the cathode material only, the diffraction peaks observed at 50.27°, 65.34°, and 70.54° were assigned to the lattices of the (114), (020), and (415) planes of α-MnO_2 (JCPDS card no. 44-0141). For the anode electrode only, diffraction peaks were observed at 14.53°, 27.01°, 67.17°, and 69.83°, which were indexed to the lattices of the (001), (220), (112), and (541) planes of the birnessite type of MnO_2 (JCPDS card no. 80-1098). The broad and strong diffraction peak at a low angle of 14.53° suggested swelled structures of the birnessite. Birnessite can exchange intercalated ions, and therefore, high electrochemical performance is expected, although the block

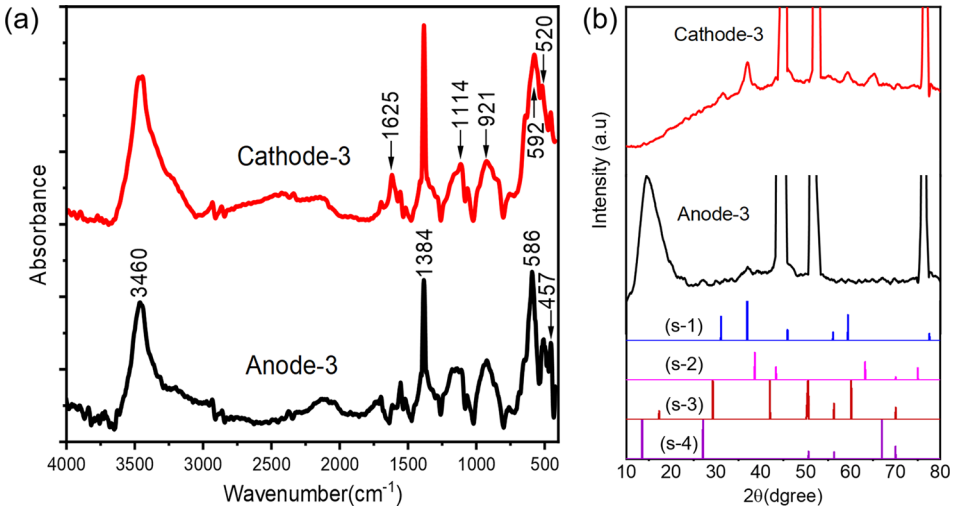

Figure 4. (a) FTIR spectra of cathode-3 and anode-3. (b) XRD patterns of cathode-3 and anode-3 with standards: (s-1) Co_3O_4, JCPDS card no. 42-1467; (s-2) NiO, JCPDS card no. 47-1049; (s-3) α-MnO_2, (JCPDS card no. 44-0141); (s-4) birnessite type of MnO_2, JCPDS card no. 80-1098.

https://doi.org/10.1021/acsomega.2c00826
ACS Omega 2022, 7, 17161−17174

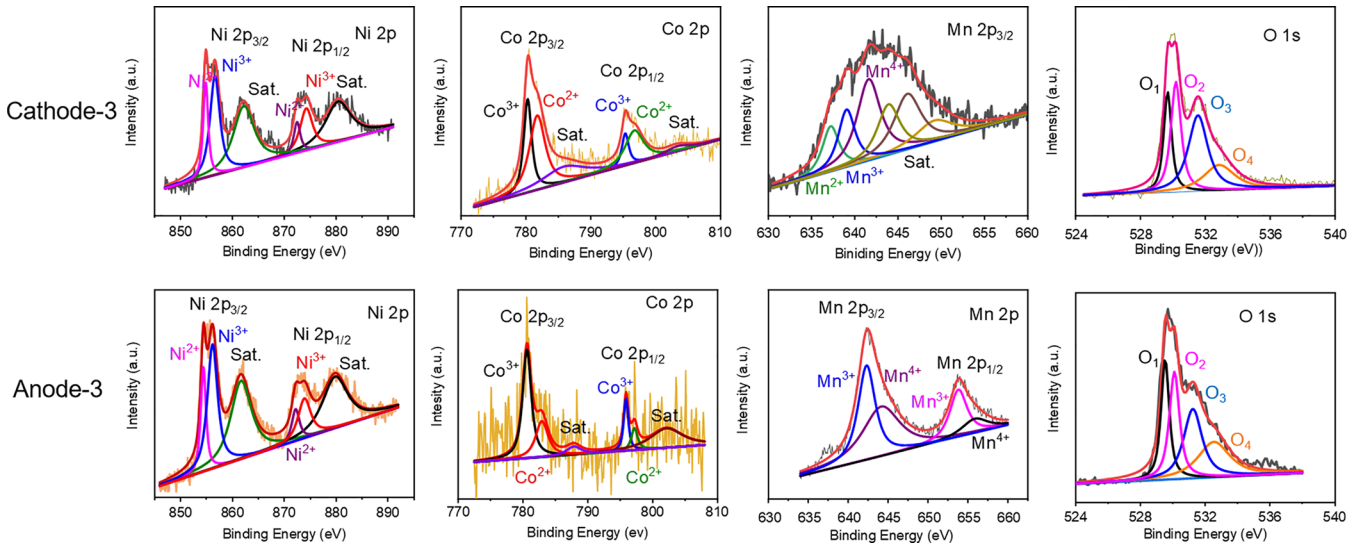

Figure 5. XPS spectra of the cathode material (upper row) and anode material (bottom row).

morphology can limit the access of ion diffusion inside. For cathode-3, the crystal size of this electrode is the grain size, which contributes to a higher specific capacitance because of the more active sites.[38]

XPS spectra were further used to examine the chemical status and elemental valence state of cathode-3 and anode-3 (Figure 5 and Tables 2 and 3). The survey spectra of both cathode-3 and anode-3 are shown in Figure S3. In the range 0−1200 eV, the Co 2p, Ni 2p, Mn 2p, and O 1s orbitals were confirmed.

Table 2. Detailed Analysis of the Deconvoluted Cathode-3 XPS Spectra

samples	species	peak position (eV)	peak area	% area
cathode-3	Ni $2p_{3/2}$ Ni^{3+}	856.64	1030.94	
	Ni $2p_{3/2}$ Ni^{2+}	854.86	504.23	
	Ni $2p_{1/2}$ Ni^{3+}	874.25	548.41	45.79
	Ni $2p_{1/2}$ Ni^{2+}	872.46	210.23	
	Sat.1	862.19	1345.88	
	Sat.2	880.39	1073.82	
	Co $2p_{3/2}$ Co^{3+}	780.27	440.81	
	Co $2p_{3/2}$ Co^{2+}	781.76	735.85	26.84
	Co $2p_{1/2}$ Co^{3+}	795.54	260.13	
	Co $2p_{1/2}$ Co^{2+}	797.42	228.54	
	Sat.1	787.21	293.94	
	Sat.2	803.66	58.75	
	Mn $2p_{3/2}$ Mn^{4+}	641.61	368.14	
	Mn $2p_{3/2}$ Mn^{3+}	639.06	187.2	13.28
	Mn $2p_{3/2}$ Mn^{2+}	637.21	146.25	
	Sat.1	643.91	220.7	
	Sat.2	646.09	290.9	
	Sat.3	649.2	153.5	

In the XPS spectra of the cathode material, the Ni 2p spectrum consisted of two main peaks at the binding energies 873.86 and 856.63 eV, which were attributed to Ni $2p_{3/2}$ and Ni $2p_{1/2}$, respectively, and two shake-up satellite peaks.[39] In detail, the Gaussian fitting peaks at the binding energies 872.23 ± 0.23 and 854.43 ± 0.43 eV were attributed to Ni^{2+}, whereas the peaks at the binding energies 873.92 ± 0.33 and 856.60 ± 0.4 eV corresponded to Ni^{3+}.[40,41] That is, the Ni hydroxides

Table 3. Detailed Analysis of Deconvoluted Anode-3 XPS Spectra

samples	species	peak position (eV)	peak area	% area
anode-3	Ni $2p_{3/2}$ Ni^{3+}	856.2	876.71	
	Ni $2p_{3/2}$ Ni^{2+}	854.43	383.78	
	Ni $2p_{1/2}$ Ni^{3+}	873.92	349.62	41.15
	Ni $2p_{1/2}$ Ni^{2+}	872.23	170.83	
	Sat.1	861.7	1123.95	
	Sat.2	879.84	895.49	
	Co $2p_{3/2}$ Co^{3+}	780.63	134.48	
	Co $2p_{3/2}$ Co^{2+}	782.99	56.63	12
	Co $2p_{1/2}$ Co^{3+}	795.89	30.72	
	Co $2p_{1/2}$ Co^{2+}	797.18	19.24	
	Sat.1	788.33	16.18	
	Sat.2	802.18	79.28	
	Mn $2p_{3/2}$ Mn^{3+}	642.32	901.18	
	Mn $2p_{3/2}$ Mn^{4+}	644.15	1018.57	27.95
	Mn $2p_{1/2}$ Mn^{3+}	653.81	451.15	
	Mn $2p_{1/2}$ Mn^{4+}	655.87	210.77	

deposited by the electrochemical reaction were partially oxidized in air during calcination, which could introduce defects into the NiO. For Co 2p, two distinct peaks at 780.38 and 795.29 eV were attributed to Co $2p_{3/2}$ and Co $2p_{1/2}$, respectively, along with two satellite (Sat.) peaks at 785.88 and 803.38 eV. The Co $2p_{3/2}$ spin orbital was decomposed into two distinct peaks located at the binding energies 780.27 ± 0.36 and 781.76 ± 0.23 eV, which were attributed to Co^{3+} and Co^{2+} cations, respectively.[40,41] Co $2p_{3/2}$ and Co $2p_{1/2}$ were separated by an energy of 14.91 eV, which indicates the presence of a Co_3O_4 cubic phase. The two satellite peaks of Co 2p at the binding energies 803.66 and 787.02 eV further confirm the presence of cobalt oxides.[42] The Co $2p_{1/2}$ spin orbital gave rise to two distinct peaks located at the binding energies 795.54 ± 0.35 and 797.42 ± 0.24 eV, which also indicated the presence of Co^{3+} and Co^{2+} cations, respectively. The Mn $2p_{3/2}$ spectrum indicated three characteristic peaks—a main peak at 641.61 eV, which was attributed to Mn^{4+}, and two peaks at the binding energies 639.06 and 637.21 eV, which were attributed to Mn^{3+} and Mn^{2+}—along with three satellite peaks at 643.91, 646.09, and 649.20 eV.[43] The high-resolution

https://doi.org/10.1021/acsomega.2c00826
ACS Omega 2022, 7, 17161−17174

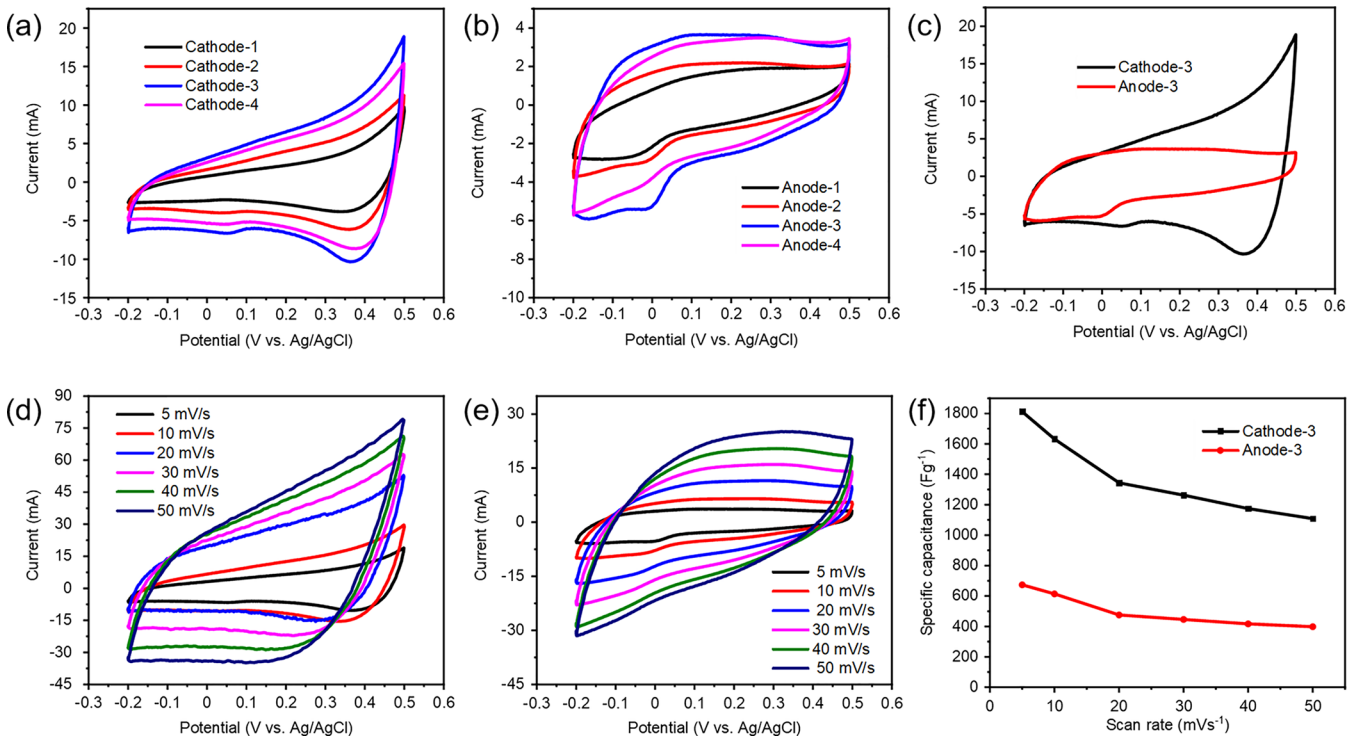

Figure 6. CV curves of (a) cathode materials and (b) anode materials scanned at 5 mV s^{-1}. (c) Comparison of the CV curves of cathode and anode materials at the scan rate 5 mV s^{-1}. CV curves of (d) cathode-3 and (e) anode-3 at different scan rates. (f) Capacitance vs scan rate.

O 1s spectrum indicated four oxygen species with the main characteristic peak at the binding energy 529.68 eV, which was ascribed to the oxygen bound to the metals. The binding energy at 530.2 eV was attributed to the adsorbed oxygen on the surface hydroxyl species. The peak at 531.54 eV was mostly related to the defect site with low oxygen coordination in the small material. The additional peak centered at 532.79 eV was related to absorbed water on the surface of defects.[41]

The presence of redox couples, Ni^{2+}/Ni^{3+} and Co^{2+}/Co^{3+}, could improve the structural stability, charge transfer efficiency, lattice parameters, thermal stability, and electrochemical performance.[44−46] The various oxidation states of Mn ions (Mn^{2+}, Mn^{3+}, and Mn^{4+}) in the cathode material could lead to high electrochemical activity for supercapacitor applications.[47] Thus, the high electrochemical performance of cathode-3 could be explained in terms of chemical states, in addition to morphological factors.

For the anode material, the peaks in the high-resolution Ni 2p spectrum were assigned to two spin−orbit doublets and two shake-up satellite peaks. The peaks at 856.2 and 874.0 eV were attributed to Ni^{3+}, and the peaks at the binding energies 854.5 and 872.2 eV corresponded to Ni^{2+}.[48] Similarly, the Co 2p spectrum contained two spin−orbit doublets. The peaks at the binding energies 780.7 and 795.8 eV were attributed to Co^{3+}, while the peaks at the binding energies 783.0 and 797.2 eV corresponded to Co^{2+}.[49] For Mn species, the spin−orbit doublet of Mn $2p_{3/2}$ was decomposed into two peaks, which were centered at 642.32 and 644.15 eV and assigned to Mn^{3+} and Mn^{4+}, respectively. The peaks at the binding energies 653.81 and 655.87 were also from Mn^{3+} and Mn^{4+}.[50] The lack of Mn^{2+} in the anode material indicated that the Mn ions were effectively oxidized during electrochemical deposition. Although Mn^{2+} was less active than the other metal ions for the anode reaction (Figure 1b), a high potential was applied to the anode, as discussed in section 3.1. This could explain why the birnessite confirmed by XRD (Figure 4b) was formed only on the anode in the same precursor solution. The chemical status of O 1s was similar to that of the cathode material.

As seen by comparing the elemental composition (% area), the ratio of Mn species was higher in the XPS results than in the EDS results (Tables 1−3). Since XPS is sensitive to the surface components, these results indicate the inhomogeneous structures of the cathode and anode materials. The surface of the active material provides contact and reactive sites in the electrochemical reactions, and this inhomogeneity of the components could affect their capacitive properties.

3.5. Electrochemical Characterization. The cathode and anode materials prepared with different mole ratios of Ni:Co:Mn were electrochemically analyzed by CV measurements at the scan rate 5 mV s^{-1} within the potential window −0.2 to 0.5 V vs Ag/AgCl in 1 M KOH aqueous electrolyte. The CV curves of both the cathode and anode materials exhibited pseudocapacitive behavior (Figure 6). Ideally, the CV curves of pseudocapacitors show rectangular shapes; however, the obtained materials exhibited deviations from the rectangular shape, suggesting several redox reactions at specific potentials. These characteristic capacitive behaviors of the materials could be attributed to the Faradaic reactions of Ni, Co, or Mn species.[47,51] The cathode and anode materials exhibited different structures in the CV curves Figure 6a and b, and as expected from the XPS results, the cathode materials, including low-valent ions, were more active under oxidative conditions (at higher potential) than the anode material Figure 6c.

In detail, cathode-1 exhibited a broad and weak reduction wave at ∼0.38 V vs Ag/AgCl. As the Co concentration in the precursor increased from 20 to 80 mM (from cathode-1 to cathode-3), the current increased, and the reduction wave

https://doi.org/10.1021/acsomega.2c00826
ACS Omega 2022, 7, 17161−17174

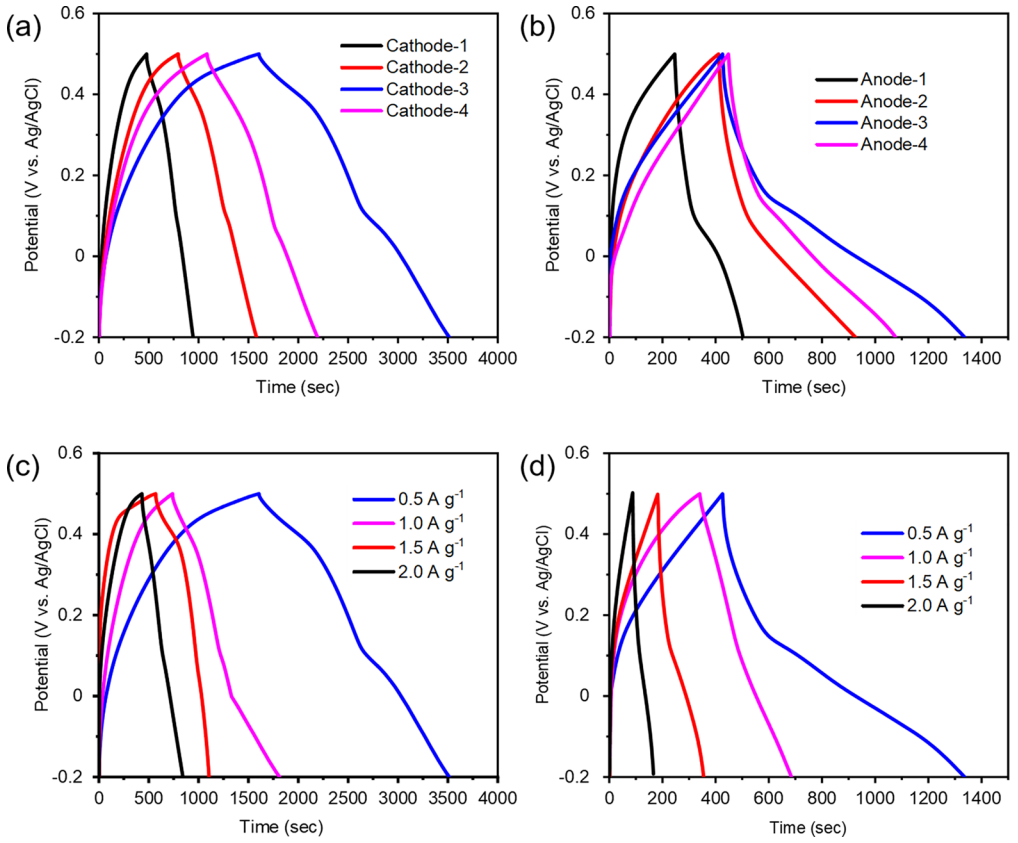

Figure 7. GCD curves of the (a) cathode and (b) anode materials at 0.5 A g^{-1} current density and (c) cathode-3 and (d) anode-3 at different current densities.

became prominent. A new reduction wave also appeared at ~0.065 V vs Ag/AgCl (Figure 6a). Thus, these reduction waves could be related to the Co species. However, the Co precursor concentration at 120 mM (cathode-4) resulted in a decrease in the reaction current. This decrease could be explained by the structural effect; that is, the thick wall of the cathode-4 film could decrease the specific surface area and then the active sites on the surface (Figure 2). Meanwhile, the anode materials showed a reduction wave at ~ −0.01 V, which increased as the Co concentration increased (Figure 6b). This wave can be associated with the reduction wave in the cathode materials at 0.065 V, although the potential was slightly changed due to the surrounding conditions (e.g., nanostructures and chemical species). The increase in Co concentration also resulted in the higher reaction current in the oxidation process, particularly in the lower potential region. This tendency was in contrast with the cathode materials: the oxidation reaction of the cathode materials was enhanced in the higher potential region by the increasing Co concentration. These differences could be explained by the valences of metallic ions in both materials (Tables 2 and 3): representatively, cathode-3 contained more Co^{2+} than Co^{3+} and, therefore, was ready to be oxidized, while the Co^{3+} was dominant in anode-3 and, therefore, the reactions in anode-3 preferentially occurred in the reductive condition. At the highest concentration of Co precursor (anode-4), the redox reactions decreased as with cathode-4.

The specific capacitance (C_s) of the active material was calculated from the CV curve using eq 1.[52]

$$C_s = \frac{1}{m\nu(V_f - V_i)} \int_{V_i}^{V_f} I(V)\, dV \quad (1)$$

where m is the mass of the active material (g), ν is the scan rate (mV s^{-1}), V_f and V_i are the final and initial potentials of the voltammetric curve (V), respectively, and I is the voltammetric current (A). The mass (m) of active material loaded on the current collector (Ni foam) was 1.7, 1.8, 1.9, and 2.1 mg for cathode-1, cathode-2, cathode-3, and cathode-4, respectively, and 2.0, 2.0, 2.3, and 2.4 mg for anode-1, anode-2, anode-3, and anode-4, respectively.

Cathode-3 exhibited the highest specific capacitance (1800 F g^{-1}) compared to cathode-1 (890 F g^{-1}), cathode-2 (1200 F g^{-1}), and cathode-4 (1400 F g^{-1}). Considering the theoretical specific capacitance of the components (3650 F g^{-1} for Co_3O_4, 2584 F g^{-1} for NiO_2, and 1370 F g^{-1} for MnO_2), cathode-3 was half pure Co_3O_4, which was rather effective as the active material in the pseudocapacitor.[53,54] The high specific capacitance of cathode-3 could be attributed to the honeycomb nanosheets (~10 nm in thickness; see Figure 2c) providing a higher specific surface area, abundant electroactive sites, and open channels that enhance the contact area between the electrolyte and electrode to improve the diffusion of electrolyte ions into the entire surface of the material.[55] Thus, the effects of Co species should be for both morphological and electrochemical aspects.

Furthermore, the specific capacitance of the anode materials was calculated to be 420, 490, 720, and 650 F g^{-1} for anode-1, anode-2, anode-3, and anode-4, respectively. These values were lower than those of the corresponding cathode materials (40−50% of the cathode materials). Anode-3 exhibited the highest

https://doi.org/10.1021/acsomega.2c00826
ACS Omega 2022, 7, 17161−17174

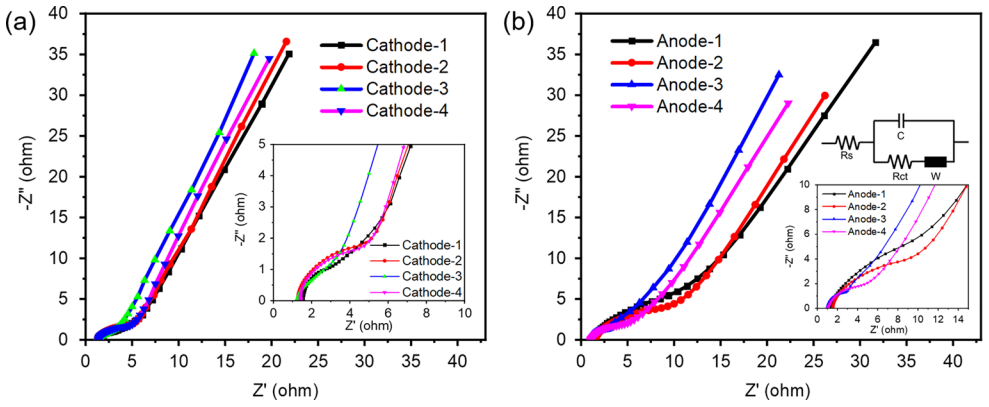

Figure 8. EIS measurements of the (a) cathode and (b) anode materials.

capacitance, which was consistent with the cathode behavior. The reduction waves at approximately 0.0 V, which were commonly observed in the cathode and anode materials, became stronger as the Co precursor concentration increased to cathode/anode-3, but the wave decreased for cathode/anode-4. At the reductive potential (in the range between −0.2 and −0.1 V), the reaction current of the anode materials was not significantly different from that of the cathode materials (Figure 6c), and the low specific capacitance of the anode materials was due to the low activity at the oxidative potentials, as mentioned above. This could indicate that the valence state of the metal ions in the TMO active material is crucial for pseudocapacitive properties. Although the redox reactions in TMOs are reversible, the material structures are arranged to stabilize their initial components in their formation processes (i.e., the deposition and calcination processes). Therefore, the deposition potential strongly affects the redox reaction of the TMOs. Since the components of both the cathode and the anode materials were not substantially different (Table 1), the morphology, chemical structure, and crystallinity of the active materials should be considered to determine the specific capacitance, as mentioned above: the block structures of the anode materials limited the surface area. The second main component in the surface of the anode material was Mn species, which theoretically possessed low capacitance, while the birnessite in the anode material could intercalate cations to enhance the non-Faradaic reaction as an EDLC.

Figure 6d depicts CV curves of cathode-3 at various scan rates from 5 to 50 mV s^{-1}. Cathode-3 exhibited quasi-rectangular loops with pseudocapacitive properties at all scan rates;[56] however, the reductive wave at ∼0.38 V decreased, and the line in the reductive process (from 0.2 to −0.2 V) became flatter as the scan rate increased. This suggests that the reduction reaction at ∼0.38 V was slower than the other energy storage mechanism in the cathode materials and could be the bottleneck of the pseudocapacitive property. Since this slow reduction process became more prominent as the Co precursor concentration increased (except for cathode-4: Figure 6a), the excess Co compounds could form an independent pathway for the redox reactions. The specific capacitance of cathode-3 declined from 1800 F g^{-1} at 5 mV s^{-1} to 1100 F g^{-1} at the scan rate 50 mV s^{-1}. On the other hand, the CV curves of anode-3 at different scan rates from 5 mV s^{-1} to 50 mV s^{-1} are also depicted in Figure 6e. The specific capacitance of anode-3 was 720 and 420 F g^{-1} at the scan rates 5 and 50 mV s^{-1}, respectively. The quasi-rectangular curve shape showed a slight distortion in the oxidation process even up to 50 mV s^{-1} except for the edges of the scan range where the switching of the oxidative/reductive processes limited the response. The reduction current was enhanced as the potential became lower, and the reduction wave at 0.065 V became less prominent. These rate dependencies were in contrast with those in cathode-3 (Figure 6d) and support the discussion on the effects of valence state. The specific capacitance at 50 mV s^{-1} was ∼60% of that at 5 mV s^{-1} for both the cathodic and anodic materials. Since the morphologies of both materials were substantially different, the rate-determining process of both materials could be Faradaic reactions, not the ion diffusion process.

Then, the electrochemical performance of both the cathode and anode materials was further investigated by GCD measurements (Figure 7). Similar to other cathode materials, cathode-3 demonstrated distinct plateaus at approximately 0.36 and 0.06 V vs Ag/AgCl, which is consistent with the redox peaks of the CV curve of cathode-3. At the current density 0.5 A g^{-1}, the cathode-3 and anode-3 nanocomposites had the longest GCD times among the series. The C_s of the active material from the GCD curve can be calculated using eq 2.

$$C_s = \frac{I\Delta t}{m\Delta V} \tag{2}$$

where m is the mass of active material (g), I is the constant current (A), Δt is the discharging time (s), and ΔV is the potential range (V).

The specific capacitance calculated from the GCD curve was 470, 620, 1400, and 750 F g^{-1} for cathode-1, cathode-2, cathode-3, and cathode-4, respectively, at the current density 0.5 A g^{-1}, while the results for anode-1, anode-2, anode-3, and anode-4 were 180, 370, 650, and 450 F g^{-1}, respectively, at the same current. This was consistent with the results obtained from CV curves. The discharging curves of cathode-3 showed very small iR drops even at a high current density of 2 A g^{-1} (Figure 7c), suggesting that the material had a low internal resistance.[57] On the other hand, the discharging curve of anode-3 at different current densities exhibited two stages: an initial fast iR drop and then a slow potential drop followed by a nonlinear slope. This behavior is consistent with the low activity of anode materials under oxidative conditions, as seen in the CV curves (Figure 6e).

To further study the electrochemical behavior of the cathode and anode materials, EIS measurements of each sample were conducted (Figure 8). In the high-frequency regions, the Nyquist plots showed semicircles, where their diameters represent the charge transfer resistance (R_{ct}) and their real

https://doi.org/10.1021/acsomega.2c00826
ACS Omega 2022, 7, 17161−17174

axis intercepts correspond to the solution resistance (R_s) of these nanocomposite electrodes. In the low-frequency region, the Nyquist plots appeared as straight lines, which represent the typical Worburg resistance (W_o). Using an equivalent circuit model, the R_{ct} values of the cathode material and the anode materials are given in Table 4. The cathode-3 electrode had good conductivity to the electrolyte, low internal resistance, and the fastest charge transfer among the electrodes, which is consistent with the highest specific capacitance of cathode-3. Considering the high R_s and R_{ct} of cathode-4, the excess Co precursor resulted in denser pores to limit surface area and ionic diffusion and probably thick walls to increase the resistance due to many defects, as shown in Figure 2. In the series of anode materials, anode-3 had the lowest R_s and R_{ct}. As shown by the larger *iR* drops in the GCD curves, the anode materials had higher R_s values than the cathode materials.[58] However, the R_{ct} values were not significantly different between the cathode and anode materials. Since the morphology of the anode materials was significantly different from that of the cathode materials, the effects of precursor components affected not only the morphology but also the microstructures for ionic diffusion and conductivity.

Table 4. R_{ct} and R_s Values of Different Electrodes and Specific Capacitances Calculated from CV Curves

electrode materials	R_{ct} (Ω)	R_s (Ω)	specific capacitance (F g^{-1})
cathode-1	1.27	1.52	890
cathode-2	1.24	1.41	1200
cathode-3	1.07	1.14	1800
cathode-4	1.12	1.32	1400
anode-1	2.56	1.58	420
anode-2	2.34	1.28	490
anode-3	1.24	1.12	720
anode-4	1.94	1.23	650

To evaluate the durability of the electrodes, their cycling properties were investigated (Figure 9). During the GCD cycles at the constant current density 10 A g^{-1}, the specific capacitance of cathode-3 decreased gradually during the first 70 cycles, which could be attributed to the partial exfoliation of active materials by a mechanical stress caused by swelling of the material during the ion diffusion process. After 2000 cycles, 90% of the initial specific capacitance of cathode-3 was retained, and its Coulombic efficiency remained above 99%. If the first 70 cycles were ignored, the specific capacitance remained at 97%. The first and last five cycles of the GCD curves (inset in Figure 9a) show similar potential−current responses, suggesting that the electrochemical response of cathode-3 was quasi-reversible. The CV curves for cathode-3 before and after the 2000 cycle test at 5 mV s^{-1} were nearly identical (Figure 9c). The calculated specific capacitance from the CV curves of cathode-3 before and after the cycle test was 1800 and 1600 F g^{-1}, respectively, and only 11% of the initial capacitance was reduced, which was consistent with the results of GCD measurements. For anode-3, the cycle stability was also investigated at the constant current density 2.2 A g^{-1}, which was much lower than that for cathode-3, for 2000 cycles (Figure 9b). The capacitance retention and Coulombic efficiency were 76% and 99%, respectively. The initial (after 70 cycles, ∼17%) and subsequent (after 1100 cycles, ∼11%) decreases in the specific capacitance were larger than those of the cathode material, which could be attributed to the blocky structure with cracks (therefore, mechanically weak in the swelling process) of the anode material (Figure 2e−h). Figure 9d shows the CV curves of anode-3 before and after the 2000 cycle test at the scan rate 5 mV s^{-1}. Both CV curves were similar; however, the reduction wave decreased in the whole

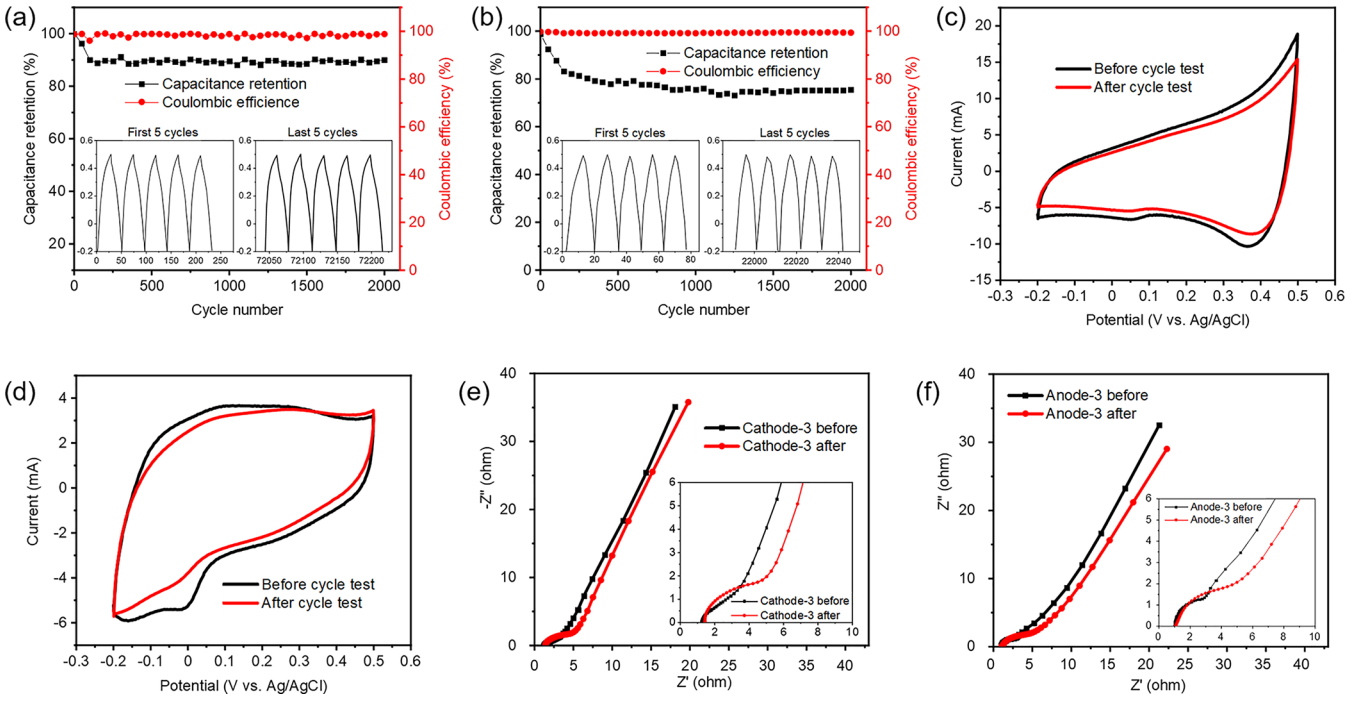

Figure 9. Capacitance retention (left axis) and Coulombic efficiency (right axis) of (a) cathode-3 and (b) anode-3, with the first five cycle (left) and last five cycle (right) GCD curves as insets. CV curves of (c) cathode-3 and (d) anode-3 before and after the cycle test. EIS analyses of (e) cathode-3 and (f) anode-3 before and after the cyclic test.

https://doi.org/10.1021/acsomega.2c00826
ACS Omega 2022, 7, 17161−17174

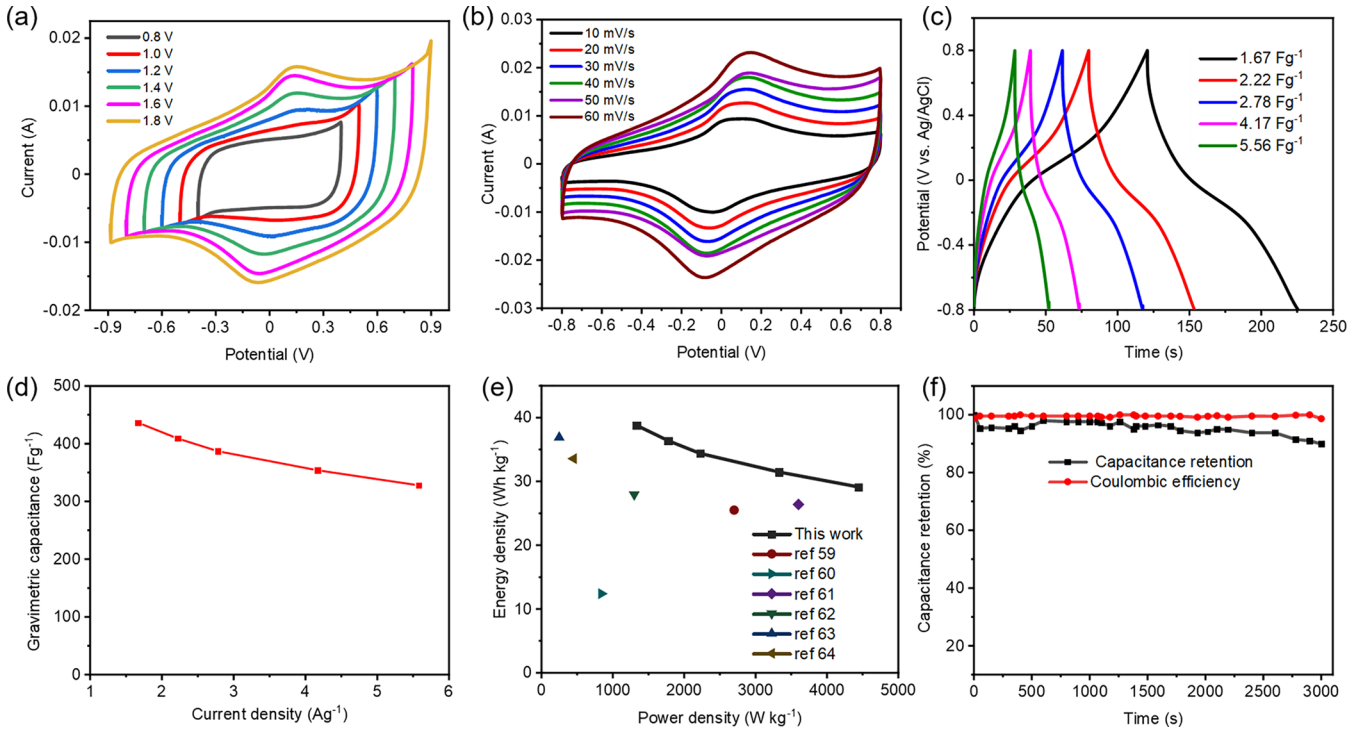

Figure 10. Electrochemical performance of the symmetric electrode system using cathode-3: CV curves (a) at different potential windows and (b) at different scan rates. (c) GCD curves at different current densities. (d) Gravimetric capacitance versus current density. (e) Ragone plots compared with reported data. (f) Cycling stability and Coulombic efficiency tested at 11.11 A g^{-1}.

region and particularly in the low-potential region (<0.08 V) after the cycling test, while the oxidation wave decreased in the range from −0.14 to 2.8 V and slightly increased at >0.35 V. These changes suggest that the repeated redox processes decreased the active sites working at low potential and probably shifted the chemical states in anode-3 to be more active in oxidative conditions. The specific capacitance decreased from 720 to 530 F g^{-1} (by ∼26%) after the cyclic test, which supported the results of the GCD measurements. EIS measurements of the cathode-3 and anode-3 electrodes were also conducted before and after the cycling stability test (Figure 9e and f). The R_s values for cathode-3 increased from 1.14 to 1.29 Ω, and the R_s values of anode-3 changed from 1.12 to 1.35 Ω after 2000 cycles. The R_s values changed more in anode-3 (increased by ∼21%) than in cathode-3 (increased by 13%). The R_{ct} values of cathode-3 changed from 1.07 to 1.14 Ω (increased by 6%), while those of anode-3 changed from 1.12 to 1.29 Ω (increased by 16%). These results suggest that the cathode material was more stable than the anode material. To investigate the structural and chemical components of the cathode and anode after cycling stability, the SEM image and EDS measurements were recorded after the 2000 cycle test (Figure S4 and Table S1). In both of the cathode and anode materials, their structures were not significantly changed: the cathode material maintained the nanosheet structure with small voids, and the anode material was blocks (see Figure 2c and g). In their chemical compositions, the ratio of oxygen seems to increase, which could be explained as the adsorption of water and a partial hydration of TMOs after the electrochemical processes in the aqueous medium (see Table 1). Considering the accuracy of the EDS measurements, substantial changes in the ratio of metallic components in these complex TMOs were not observed.

Thus, a simple preparation method of complex TMOs (Ni, Co, and Mn) and their electrochemical properties were studied. From an aqueous solution of the precursor mixture, nanostructured TMOs were deposited on both the cathode and the anode via different reaction processes. The structures of the obtained TMOs were different between the cathode and anode and further changed by adjusting the mixing ratio of the precursors. The electrochemical performance of the obtained TMOs was also changed by adjusting the cathode/anode and mixing ratio. The cathode material with a proper mixing ratio resulted in a very high specific capacitance (1800 F g^{-1}) and sufficient stability. This approach can be applicable and useful for designing complex TMOs for pseudocapacitors and other electrochemical applications.

3.6. Electrochemical Measurement of the Two Electrode System. The symmetric electrode system was fabricated by assembling two cathode-3 electrodes with a filter paper separator to test the practical performance of supercapacitors (Figure 10). In the potential window ranging from ±0.4 to ±0.5 V, the CV curves were rectangular shapes (Figure 10a). When the potential range increased from ±0.6 to ±0.8 V, the CV curves exhibited broad anodic and cathodic peaks centered at ∼0.12 and −0.056 V, which was attributed to reversible redox reactions. As the operating potential window increased, the current intensity of the anodic and cathodic peaks increased, and the peak positions shifted toward lower potentials. When the potential range increased to ±0.9 V, the CV curve exhibited a sharp peak around 0.9 V, which suggests water decomposition.[14,15] Thus, we chose the potential range ±0.8 V as the operating potential window for the symmetric supercapacitor working with aqueous electrolyte. At different scan rates, the shapes of the CV curves were nearly the same, and the current response was enhanced with a shift in peak positions toward more positive (oxidation peak) and more

https://doi.org/10.1021/acsomega.2c00826
ACS Omega 2022, 7, 17161−17174

negative (reduction peak) as the scan rate increased (Figure 10b). The GCD measurements were also conducted in the potential range ±0.8 V at different current densities from 1.67 to 5.56 A g^{-1} (Figure 10c). The GCD curve exhibited potential plateaus at approximately 0 V, which corresponded to the redox peaks in the CV curves.

Then, the gravimetric capacitance (C_g), energy density (E), and power density (P) of the symmetric electrode system were calculated using the formulas given in eqs 3−5, respectively.[59]

$$C_g = \frac{4I\Delta t}{m\Delta V} \quad (3)$$

$$E = \frac{0.5C_g(\Delta V)^2}{4 \times 3.6} \quad (4)$$

$$P = \frac{E}{\Delta t}3600 \quad (5)$$

where C_g is the gravimetric capacitance (F g^{-1}), I is the discharging current (A), Δt is the discharging time (s), m is the total mass (3.8 mg) of active material on both the positive electrode (m^+) and negative electrode (m^-) (g), ΔV is the potential window (V), E is the energy density (Wh kg^{-1}), and P is the power density (W kg^{-1}). The specific capacitance calculated from the GCD curve at 1.67 A g^{-1} was 440 F g^{-1} and decreased to 330 F g^{-1} at 5.56 A g^{-1} with a good capacitance retention of 75% (Figure 10d). At a higher scan rate, the limitation of ion diffusion decreased the specific capacitance, as observed above in the characterization of cathode-3. As indicated in the Ragone plots (Figure 10e), the symmetric electrode system demonstrated a high energy density of 39 W h kg^{-1} and a power density of 1300 W kg^{-1} at the current density 1.67 A g^{-1}. When the current density reached 5.58 A g^{-1}, the energy density was 29 Wh kg^{-1}, and the power density was 4400 W kg^{-1}. These relations between the energy and power density of the symmetric electrode system in this study were higher than those of the other systems reported previously.[59−64] This high performance could be due to the high activity of cathode-3 in the wide operational potential window (i.e., 1.6 V). The cycle stability was tested at a high current density of 11 A g^{-1} for 3000 GCD cycles in the potential range ±0.8 V (Figure 10f). After 3000 cycles, the capacitance retention was 90% of the initial specific capacitance, and the Coulombic efficiency was 99%, indicating a sufficient cycle stability and reversibility of the symmetric electrode system designed in this study.

4. CONCLUSION

Binder-free electrodes consisting of complex TMOs on Ni foam were simultaneously prepared from mixtures of Ni, Co, and Mn nitrates using a simple and cost-effective electrodeposition approach. The deposited materials on both the cathode (which required a thermal treatment to oxidize to TMOs) and the anode exhibited different nanostructures: nanosheets on the cathode and blocks on the anode. Their electrochemical performance changed as the molar ratio of Co:Ni:Mn varied from 0.5:2:1 to 3:2:1. The cathode material prepared from the electrolyte of Co:Ni:Mn = 2:2:1 (cathode-3) exhibited the highest specific capacitance in the series, namely, 1800 F g^{-1} at 5 mV s^{-1} from the CV curve and 1400 F g^{-1} at the current density 0.5 A g^{-1} from the GCD curve, and excellent cycling stability of 90% after 2000 cycles. Such a high electrochemical performance of cathode-3 is related to the desirable molar ratio of Ni:Mn:Co, synergetic effect, and morphological characteristics of a suitable interconnected thin and long nanosheet structure with open space between each nanosheet, which provides more electroactive sites for redox reactions and facilitates the rate of electron and ion transport, which can increase the conductivity of the electrode. Moreover, the coexistence of three different cations in a single electrode may contribute more electrons than electrodes with only single-metal oxides, which shows electrical conductivity and electrochemical performance improvements. The prominent electrochemical properties and synthetic method (simplicity, low cost, and reproducibility) should make the cathode-3 nanosheet architecture a promising electrode for next-generation supercapacitors.

■ ASSOCIATED CONTENT

Supporting Information

The Supporting Information is available free of charge at https://pubs.acs.org/doi/10.1021/acsomega.2c00826.

Figure S1. Cathode material before (A) and after (B) heat treatment. Figure S2. Anode material before (A) and after (B) heat treatment. Figure S3. Survey XPS spectra of cathode-3 and anode-3. Figure S4. SEM images of cathode-3 (A1) and anode-3 (B1) after the 2000 cycle test and their corresponding EDS analyses. Table S1. Elemental compositions of the cathode and anode materials after the cycle test. (PDF)

■ AUTHOR INFORMATION

Corresponding Author

Masaki Ujihara − *Graduate Institute of Applied Science and Technology, National Taiwan University of Science and Technology, Taipei 10607 Taiwan, Republic of China;* orcid.org/0000-0003-2961-413X; Phone: +886-2-2730-3773; Email: masaki.ujihara@mail.ntust.edu.tw

Author

Eshetu Mekonnen Abebe − *Graduate Institute of Applied Science and Technology, National Taiwan University of Science and Technology, Taipei 10607 Taiwan, Republic of China*

Complete contact information is available at: https://pubs.acs.org/10.1021/acsomega.2c00826

Notes

The authors declare no competing financial interest.

■ ACKNOWLEDGMENTS

This investigation was partly supported by the Ministry of Science and Technology of the Republic of China (MOST 109-2221-E-011-062) and Graduate Institute of Applied Science and Technology, National Taiwan University of Science and Technology.

■ REFERENCES

(1) Zijiong, L.; Weiyang, Z.; Yanyue, L.; Jinjin, G.; Baocheng, Y. 2D nickel oxide nanosheets with highly porous structure for high performance capacitive energy storage. *J. Phys.: Applied Physics* **2018**, *51*, 045302.

(2) Zhong, J.-H.; Wang, A.-L.; Li, G.-R.; Wang, J.-W.; Ou, Y.-N.; Tong, Y.-X. Co_3O_4/$Ni(OH)_2$ composite mesoporous nanosheet networks as a promising electrode for supercapacitor applications. *J. Mater. Chem.* **2012**, *22*, 5656−5665.

(3) Mensah-Darkwa, K.; Zequine, C.; Kahol, P.; Gupta, R. Supercapacitor energy storage device using biowastes: A sustainable approach to green energy. *Sustainability* **2019**, *11*, 414.
(4) Li, X.; Miao, R.; Tao, B.; Miao, F.; Zang, Y.; Chu, P. K. Co_3O_4/MnO_2/$Co(OH)_2$ on nickel foam composites electrode with excellent electrochemical performance for supercapacitor. *Solid State Sci.* **2019**, *95*, 105941.
(5) Patrice, S.; Yury, G. Materials for electrochemical capacitors. *Nanosci. Technol.* **2009**, 320−329.
(6) Zaharaddeen, S. I.; Subramani, C.; Dash, S. S. A brief review on electrode materials for supercapacitor. *Int. J. Electrochem. Sci.* **2016**, *11*, 10628−10643.
(7) Naskar, P.; Maiti, A.; Chakraborty, P.; Kundu, D.; Biswas, B.; Banerjee, A. Chemical supercapacitors: a review focusing on metallic compounds and conducting polymers. *J. Mater. Chem. A* **2021**, *9*, 1970−2017.
(8) Elkholy, A. E.; El-Taib Heakal, F.; Allam, N. K. A facile electrosynthesis approach of amorphous Mn-Co-Fe ternary hydroxides as binder-free active electrode materials for high-performance supercapacitors. *Electrochim. Acta* **2019**, *296*, 59−68.
(9) Liang, R.; Du, Y.; Xiao, P.; Cheng, J.; Yuan, S.; Chen, Y.; Yuan, J.; Chen, J. Transition metal oxide electrode materials for supercapacitors: A review of recent developments. *Nanomaterials* **2021**, *11*, 1248.
(10) Shinde, P. A.; Jun, S. C. Review on recent progress in the development of tungsten oxide based electrodes for electrochemical energy storage. *ChemSusChem* **2020**, *13*, 11−38.
(11) Debelo, T. T.; Ujihara, M. Effect of simultaneous electrochemical deposition of manganese hydroxide and polypyrrole on structure and capacitive behavior. *J. Electroanal. Chem.* **2020**, *859*, 113825.
(12) Seok, D.; Jeong, Y.; Han, K.; Yoon, D. Y.; Sohn, H. Recent progress of electrochemical energy devices: Metal oxide−carbon nanocomposites as materials for next-generation chemical storage for renewable energy. *Sustainability* **2019**, *11*, 3694.
(13) Rusi, S. R.; Majid. Electrodeposited Mn_3O_4-NiO-Co_3O_4 as a composite electrode material for electrochemical capacitor. *Electrochim. Acta* **2015**, *175*, 193−201.
(14) Wang, Z.; Shen, S.; Lin, Z.; Tao, W.; Zhang, Q.; Meng, F.; Gu, L.; Zhong, W. Regulating the Local Spin State and Band Structure in Ni_3S_2 Nanosheet for Improved Oxygen Evolution Activity. *Adv. Funct. Mater.* **2022**, *32*, 2112832.
(15) Shen, S.; Wang, Z.; Lin, Z.; Song, K.; Zhang, Q.; Meng, F.; Gu, L.; Zhong, W. Crystalline-Amorphous Interfaces Coupling of $CoSe_2$/CoP with Optimized d-Band Center and Boosted Electrocatalytic Hydrogen Evolution. *Adv. Mater.* **2022**, *34*, 2110631.
(16) Li, L.; Zhang, Y.; Shi, F.; Zhang, Y.; Zhang, J.; Gu, C.; Wang, X.; Tu, J. Spinel manganese−nickel−cobalt ternary oxide nanowire array for high-performance electrochemical capacitor applications. *ACS Appl. Mater. Interfaces* **2014**, *6*, 18040−18047.
(17) She, Y.; Tang, B.; Li, D.; Tang, X.; Qiu, J.; Shang, Z.; Hu, W. Mixed nickel-cobalt-molybdenum metal oxide nanosheet arrays for hybrid supercapacitor applications. *Coatings* **2018**, *8*, 340.
(18) Xu, K.; Zou, R.; Li, W.; Xue, Y.; Song, G.; Liu, Q.; Liu, X.; Hu, J. Self-assembling hybrid NiO/Co_3O_4 ultrathin and mesoporous nanosheets into flower-like architectures for pseudocapacitance. *J. Mater. Chem. A* **2013**, *1*, 9107−9113.
(19) Zeng, Z.; Xiao, B.; Zhu, X.; Zhu, J.; Xiao, D.; Zhu, J. Flower-like binary cobalt-nickel oxide with high performance for supercapacitor electrode via cathodic electrodeposition. *Ceram. Int.* **2017**, *43*, S633−S638.
(20) Abebe, E. M.; Ujihara, M. Influence of temperature on ZnO/Co_3O_4 nanocomposites for high energy storage supercapacitors. *ACS Omega* **2021**, *6*, 23750−23763.
(21) Nayak, P. K.; Munichandraiah, N. Simultaneous electrodeposition of MnO_2 and $Mn(OH)_2$ for supercapacitor studies. *Electrochem. Solid-State Lett.* **2009**, *12*, A115.
(22) Wang, H.; Ren, Q.; Brett, D. J.; He, G.; Wang, R.; Key, J.; Ji, S. Double-shelled tremella-like NiO@Co_3O_4@MnO_2 as a high-performance cathode material for alkaline supercapacitors. *J. Power Sources* **2017**, *343*, 76−82.
(23) Biswal, A.; Panda, P. K.; Acharya, A. N.; Mohapatra, S.; Swain, N.; Tripathy, B. C.; Jiang, Z. T.; Minakshii Sundaram, S. Role of additives in electrochemical deposition of ternary metal oxide microspheres for supercapacitor applications. *ACS Omega* **2020**, *5*, 3405−3417.
(24) Shaban, M.; Kholidy, I.; Ahmed, G. M.; Negem, M.; Abd El-Salam, H. M. Cyclic voltammetry growth and characterization of Sn−Ag alloys of different nanomorphologies and compositions for efficient hydrogen evolution in alkaline solutions. *RSC Adv.* **2019**, *9*, 22389−22400.
(25) Cardoso, D. P.; Amaral, L.; Santos, D. M.; Šljukić, B.; Sequeira, C. A. C.; Macciò, D.; Saccone, A. Enhancement of hydrogen evolution in alkaline water electrolysis by using nickel-rare earth alloys. *Int. J. Hydrog. Energy* **2015**, *40*, 4295−4302.
(26) Xu, Q. Z.; Su, Y. Z.; Wu, H.; Cheng, H.; Hui, Y. P.; Li, N.; Liu, Z. Q. Effect of morphology of Co_3O_4 for oxygen evolution reaction in alkaline water electrolysis. *Curr. Nanosci* **2014**, *11*, 107−112.
(27) Behazin, M.; Biesinger, M. C.; Noël, J. J.; Wren, J. C. Comparative study of film formation on high-purity Co and Stellite-6: Probing the roles of a chromium oxide layer and gamma-radiation. *Corros. Sci.* **2012**, *63*, 40−50.
(28) Gu, L.; Wang, Y.; Lu, R.; Guan, L.; Peng, X.; Sha, J. Anodic electrodeposition of a porous nickel oxide−hydroxide film on passivated nickel foam for supercapacitors. *J. Mater. Chem. A* **2014**, *2*, 7161−7164.
(29) Li, D.; Ren, B.; Jin, Q.; Cui, H.; Wang, C. Nitrogen-doped, oxygen-functionalized, edge- and defect-rich vertically aligned graphene for highly enhanced oxygen evolution reaction. *J. Mater. Chem. A* **2018**, *6*, 2176−2183.
(30) Yang, Q.; Lu, Z.; Sun, X.; Liu, J. Ultrathin Co_3O_4 nanosheet arrays with high supercapacitive performance. *Sci. Rep.* **2013**, *3*, 3537.
(31) Liu, F.; Su, H.; Jin, L.; Zhang, H.; Chu, X.; Yang, W. Facile synthesis of ultrafine cobalt oxide nanoparticles for high-performance supercapacitors. *J. Colloid Interface Sci.* **2017**, *505*, 796−804.
(32) Racik, K. M.; Guruprasad, K.; Mahendiran, M.; Madhavan, J.; Maiyalagan, T.; Raj, M. V. A. Enhanced electrochemical performance of MnO_2/NiO nanocomposite for supercapacitor electrode with excellent cycling stability. *J. Mater. Sci.: Mater. Electron.* **2019**, *30*, 5222−5232.
(33) Huang, M.; Zhang, Y.; Li, F.; Zhang, L.; Ruoff, R. S.; Wen, Z.; Liu, Q. Self-assembly of mesoporous nanotubes assembled from interwoven ultrathin birnessite-type MnO_2 nanosheets for asymmetric supercapacitors. *Sci. Rep.* **2015**, *4*, 3878.
(34) Ardila Rodriguez, L. A.; Travessa, D. N. Core/Shell structure of TiO_2-Coated MWCNTs for thermal protection for high-temperature processing of metal matrix composites. *Adv. Mater. Sci. Eng.* **2018**, *2018*, 7026141.
(35) Gupta, N. K.; Saifuddin, M.; Kim, S. Microscopic, spectroscopic, and experimental approach towards understanding the phosphate adsorption onto Zn−Fe layered double hydroxide. *J. Mol. Liq.* **2020**, *297*, 11935.
(36) Xia, X. H.; Tu, J. P.; Mai, Y. J.; Wang, X.; Gu, C. D.; Zhao, X. B. Self-supported hydrothermal synthesized hollow Co_3O_4 nanowire arrays with high supercapacitor capacitance. *J. Mater. Chem.* **2011**, *21*, 9319−9325.
(37) Sadiq, M. M. J.; Nesaraj, A. S. Development of NiO-Co_3O_4 nano-ceramic composite materials as novelphotocatalysts to degrade organic contaminants present in water. *Int. J. Environ. Res.* **2014**, *8*, 1171−1184.
(38) Liu, X.; Chen, G.; Guan, H.; Dong, C.; Xiao, X.; Wang, Y. Binder-free NiO@MnO_2 core-shell electrode: Rod-like NiO core prepared through corrosion by oxalic acid and enhanced pseudocapacitance with sphere-like MnO_2 shell. *Electrochim. Acta* **2016**, *189*, 83−92.
(39) Zhao, X.; Liu, X.; Li, F.; Huang, M. MnO_2@NiO nanosheets@nanowires hierarchical structures with enhanced supercapacitive properties. *J. Mater. Sci.* **2020**, *55*, 2482−2491.

https://doi.org/10.1021/acsomega.2c00826
ACS Omega 2022, 7, 17161−17174

(40) Ashok, A.; Kumar, A.; Ponraj, J.; Mansour, S. A.; Tarlochan, F. Single step synthesis of porous $NiCoO_2$ for effective electrooxidation of glycerol in alkaline medium. *J. Electrochem. Soc.* **2018**, *165*, J3301−J3309.
(41) Liu, X.; Hao, C.; Jiang, H.; Zeng, M.; Yu, R. Hierarchical $NiCo_2O_4/Co_3O_4/NiO$ porous composite: a lightweight electromagnetic wave absorber with tunable absorbing performance. *J. Mater. Chem. C* **2017**, *5*, 3770−3778.
(42) Smyrnioti, M.; Ioannides, T. Synthesis of cobalt-based nanomaterials from organic precursors. *Cobalt* **2017**, 49.
(43) Ni, L.; Wu, Z.; Zhao, G.; Sun, C.; Zhou, C.; Gong, X.; Diao, G. Core−shell structure and interaction mechanism of γ-MnO_2 coated sulfur for improved lithium-sulfur batteries. *Small* **2017**, *13*, 1603466.
(44) Sun, H.; Zhao, K. Electronic structure and comparative properties of $LiNi_xMn_yCo_zO_2$ cathode materials. *J. Phys. Chem. C* **2017**, *121*, 6002−6010.
(45) Sun, Y.; Zuo, X.; Xu, D.; Sun, D.; Zhang, X.; Zeng, S. Flower−like $NiCo_2O_4$ Microstructures as promising anode material for high performance lithium-ion batteries: Facile synthesis and its lithium storage properties. *ChemistrySelect* **2016**, *1*, 5129−5136.
(46) Liang, J.; Fan, Z.; Chen, S.; Ding, S.; Yang, G. Hierarchical $NiCo_2O_4$ nanosheets@halloysite nanotubes with ultrahigh capacitance and long cycle stability as electrochemical pseudocapacitor materials. *Chem. Mater.* **2014**, *26*, 4354−4360.
(47) He, P.; Huang, Q.; Huang, B.; Chen, T. Controllable synthesis of Ni−Co−Mn multi-component metal oxides with various morphologies for high-performance flexible supercapacitors. *RSC Adv.* **2017**, *7*, 24353−24358.
(48) Mahala, C.; Basu, M. Nanosheets of $NiCo_2O_4$/NiO as efficient and stable electrocatalyst for oxygen evolution reaction. *ACS omega* **2017**, *2*, 7559−7567.
(49) Liu, W.; Li, M.; Zhou, W.; Zhu, Y. MOF-derived Co_3O_4 nanoparticles embedded in NiO nanosheet arrays as heterostructure cathode for rechargeable lithium-oxygen batteries. *Ionics* **2021**, *27*, 2915−2925.
(50) Chen, K.; Wang, M.; Li, G.; He, Q.; Liu, J.; Li, F. Spherical α-MnO_2 supported on N-KB as efficient electrocatalyst for oxygen reduction in Al−air battery. *Materials* **2018**, *11* (4), 601.
(51) Wang, R.; Yan, X. Superior asymmetric supercapacitor based on Ni-Co oxide nanosheets and carbon nanorods. *Sci. Rep.* **2015**, *4*, 3712.
(52) Jia, W.; Li, J.; Lu, Z.; Juan, Y.; Jiang, Y. Synthesis of honeycomb-like Co_3O_4 nanosheets with excellent supercapacitive performance by morphological controlling derived from the alkaline source ratio. *Materials* **2018**, *11*, 1560.
(53) Xu, K.; Zou, R.; Li, W.; Xue, Y.; Song, G.; Liu, Q.; Liu, X.; Hu, J. Self-assembling hybrid NiO/Co_3O_4 ultrathin and mesoporous nanosheets into flower-like architectures for pseudocapacitance. *J. Mater. Chem. A* **2013**, *1*, 9107−9113.
(54) Saykar, N. G.; Pilania, R. K.; Banerjee, I.; Mahapatra, S. Synthesis of $NiO−Co_3O_4$ nanosheet and its temperature-dependent supercapacitive behavior. *J. Phys.: Applied Physics* **2018**, *51*, 475501.
(55) Shinde, S. K.; Ramesh, S.; Bathula, C.; Ghodake, G. S.; Kim, D. Y.; Jagadale, A. D.; Kadam, A. A.; Waghmode, D. P.; Sreekanth, T. V. M.; Kim, H. S.; Nagajyothi, P. C.; Yadav, H. M. Novel approach to synthesize $NiCo_2S_4$ composite for high-performance supercapacitor application with different molar ratio of Ni and Co. *Sci. Rep.* **2019**, *9*, 13717.
(56) Rosaiah, P.; Zhu, J.; Hussain, O. M.; Qiu, Y. Synthesis of flower-like reduced graphene oxide−Mn_3O_4 nanocomposite electrodes for supercapacitors. *Appl. Phys. A: Mater. Sci. Process.* **2018**, *124*, 597.
(57) Sun, G.; Yang, H.; Zhang, G.; Gao, J.; Jin, X.; Zhao, Y.; Jiang, L.; Qu, L. A capacity recoverable zinc-ion micro-supercapacitor. *Energy Environ. Sci.* **2018**, *11*, 3367−3374.
(58) Kim, B. K.; Sy, S.; Yu, A.; Zhang, J. Electrochemical supercapacitors for energy storage and conversion. In *Handbook of Clean Energy Systems.*; Yan, J. Y., Ed.; John Wiley & Sons: Hoboken, 2015; pp 1−25.
(59) Sundriyal, S.; Shrivastav, V.; Kaur, H.; Mishra, S.; Deep, A. High-performance symmetrical supercapacitor with a combination of a ZIF-67/rGO composite electrode and a redox additive electrolyte. *ACS omega* **2018**, *3*, 17348−17358.
(60) Jiang, J.; Sun, Y.; Chen, Y.; Hu, X.; Zhu, L.; Chen, H.; Han, S. One-step synthesis of nickel cobalt sulfide nanostructure for high-performance supercapacitor. *J. Mater. Sci.* **2019**, *54*, 11936−11950.
(61) Kumar, A.; Sanger, A.; Kumar, A.; Mishra, Y. K.; Chandra, R. Performance of high energy density symmetric supercapacitor based on sputtered MnO_2 nanorods. *ChemistrySelect* **2016**, *1*, 3885−3891.
(62) Raphael Ezeigwe, E.; Dong, L.; Wang, J.; Wang, L.; Yan, W.; Zhang, J. MOF-deviated zinc-nickel−cobalt ZIF-67 electrode material for high-performance symmetrical coin-shaped supercapacitors. *J. Colloid Interface Sci.* **2020**, *574*, 140−151.
(63) Li, C.; Wu, W.; Wang, P.; Zhou, W.; Wang, J.; Chen, Y.; Fu, L.; Zhu, Y.; Wu, Y.; Huang, W. Fabricating an aqueous symmetric supercapacitor with a stable high working voltage of 2 V by using an alkaline−acidic electrolyte. *Adv. Sci.* **2019**, *6*, 1801665.
(64) Sarmah, D.; Kumar, A. Symmetric Supercapacitors with layer-by-layer Molybdenum disulfide reduced graphene oxide structures and poly(3,4-ethylenedioxythiophene) nanoparticles nanohybrid electrode. *J. Energy Storage* **2021**, *35*, 102289.

https://doi.org/10.1021/acsomega.2c00826
ACS Omega 2022, 7, 17161−17174